*electronics*

MDPI

*Article*

# Dynamic Imprint and Recovery Mechanisms in $Hf_{0.2}Zr_{0.8}O_2$ Anti-Ferroelectric Capacitors with FORC Characterization

**Yuetong Huo [1], Jianguo Li [2], Zeping Weng [3], Yaru Ding [4], Lijian Chen [2,4], Jiabin Qi [2], Yiming Qu [2,*] and Yi Zhao [2,*]**

[1] School of Integrated Circuits, East China Normal University, Shanghai 200241, China; 71265900007@stu.ecnu.edu.cn
[2] Research Center of Integrated Circuits, Huada Semiconductor, Shanghai 201203, China; lijg@hdsc.com.cn (J.L.); 22331054@zju.edu.cn (L.C.); qijb@hdsc.com.cn (J.Q.)
[3] State Key Laboratory of Silicon and Advanced Semiconductor Materials, Zhejiang University, Hangzhou 310027, China; wengzp@zju.edu.cn
[4] College of Information Science and Electronic Engineering, Zhejiang University, Hangzhou 310027, China; dingyaru@zju.edu.cn
* Correspondence: quym@hdsc.com.cn (Y.Q.); zhaoyi@hdsc.com.cn (Y.Z.)

**Abstract**

The conventional static imprint effect in $Hf_xZr_{1-x}O_2$ (HZO) ferroelectric (FE) devices, which degrades data retention, is generally characterized by a shift in the hysteresis loop along the electric field axis. Unlike the static imprint effect, the dynamic imprint effect emerges under dynamic electric fields or actual operating conditions, making the FE film exceptionally sensitive to switching pulse parameters and domain history. In HZO anti-ferroelectric (AFE) devices, this dynamic imprint effect alters the coercive field distribution associated with domain switching and poses a significant challenge to long-term stable device operation. This study systematically investigates the dynamic imprint effect and its recovery process using a comprehensive integration of first-order reversal curve (FORC) analysis, transient current-voltage (I-V), and polarization-voltage (P-V) characterization. By analyzing localized imprint behavior under sub-cycling conditions, mechanisms and recovery pathways of imprint in AFE devices are proposed. Finally, possible physics-based mechanisms describing imprint behaviors and recovery behaviors are discussed, providing insights for optimizing AFE memory technology performance and reliability.

**Keywords:** anti-ferroelectric; FORC; sub-cycling; split-up; imprint; recovery

check for updates

Academic Editor: Ray-Hua Horng

Received: 7 October 2025
Revised: 6 November 2025
Accepted: 20 November 2025
Published: 23 November 2025

**Citation:** Huo, Y.; Li, J.; Weng, Z.; Ding, Y.; Chen, L.; Qi, J.; Qu, Y.; Zhao, Y. Dynamic Imprint and Recovery Mechanisms in $Hf_{0.2}Zr_{0.8}O_2$ Anti-Ferroelectric Capacitors with FORC Characterization. *Electronics* **2025**, *14*, 4593. https://doi.org/10.3390/electronics14234593

**Copyright:** © 2025 by the authors. Licensee MDPI, Basel, Switzerland. This article is an open access article distributed under the terms and conditions of the Creative Commons Attribution (CC BY) license (https://creativecommons.org/licenses/by/4.0/).

## 1. Introduction

In emerging non-volatile memory (NVM) technologies, Hf-based ferroelectric memories have attracted attention due to the characteristics of hafnium zirconium oxide (HZO, $Hf_xZr_{1-x}O_2$) materials. HZO is environmentally benign, lead-free, and compatible with the miniaturization of complementary metal-oxide semiconductor (CMOS) technology. These features make it suitable for large-scale production. However, there are still reliability issues that need to be studied and addressed, with device degradation caused by imprint effects has proven to be one of the most critical problems [1,2]. Studies have shown that imprint effects can lead to issues such as read/write errors and reduced data retention time during the durability process, posing a significant challenge for long-term stable operation [3].

The conventional imprint effect generally refers to the phenomenon where the hysteresis curve of ferroelectric (FE) devices shifts along the electric field axis [4]. This effect

is typically characterized by a preferential orientation of one polarization state relative to another [5], resulting in asymmetric polarization in the ferroelectric film. This phenomenon affects the memory window, ultimately leading to higher operating voltages and shortened retention time [6], which in turn impacts the reliability of data and storage [7]. Charge injection and trapping have become the mainstream hypothesis for the conventional imprint effect [6]. However, its specific physical mechanism remains a topic of ongoing debate.

Unlike conventional imprints, the dynamic imprint effect is characterized by much faster dynamics, leading to an imprint state that is easily modifiable and recoverable. The dynamic imprint effect is primarily observed under dynamic electric fields (such as frequently switched fields) or actual operating conditions [8], is the key factor affecting device endurance. This behavior is highly sensitive to the parameters of the switching pulses and the domain state history of the ferroelectric thin film [9]. The underlying mechanism is thought to be attributed to electron injection and the tunneling effect. Furthermore, during the endurance cycling process, partial electron de-trapping recovery also occurs.

Hf-based anti-ferroelectric (AFE) memories, due to their low switching field and superior endurance compared to ferroelectric materials, are promising in the application of embedded dynamic random-access memory (eDRAM) [10,11]. However, the mechanisms behind the imprint effect in AFE films are still unclear and require further investigation.

Beyond the traditional polarization-voltage (P-V) and transient current-voltage (I-V) tests, the technique of first-order reversal curves (FORC) is generally used for in-depth study of the switching behavior, non-uniformity, interaction, and energy distribution of FE/AFE domains. Based on the Preisach model, it exhibits the memorizing characteristic, which is similar to the imprint behavior of the ferroelectric film when an electric field is applied. Moreover, FORC test plots can visually reflect the coercive field and internal bias field evolution of the FE/AFE film [12–14]. This approach aids in a deeper analysis of the imprint effect and its recovery behavior in the HZO AFE film [15].

In this study, the FORC-assisted characterizations have been adopted to investigate the dynamic imprint and its recovery behavior under the external electric field cycling in AFE memories. By combining transient I-V curves with FORC test plots, the underlying mechanisms are explored. Furthermore, based on previous literature reports and the understanding of the imprint effect and recovery mechanisms in the AFE film, possible physical mechanisms for the imprint effect and its recovery behavior are proposed.

## 2. Experiments

### *2.1. Device Processing*

The sample used in this work is a W/TiN/$Hf_{0.2}Zr_{0.8}O_2$/TiN structure, as schematically shown in Figure 1a. The Metal-Antiferroelectric-Metal (MFM) capacitor devices were fabricated on the heavily doped $p^+$ Si substrate. The 10 nm thick TiN and 8 nm $Hf_{0.2}Zr_{0.8}O_2$ film were deposited by ALD (Atomic Layer Deposition). By adjusting the cycle ratio of the two precursors, the Hf:Zr ratio was carefully controlled to 1:4 and confirmed through XPS (X-ray Photoelectron Spectroscopy). Then, the samples were processed with RTA (Rapid Thermal Annealing) at 450 °C in $N_2$. More fabrication details are described in [16]. The electrical tests were conducted using the F3000 ferroelectric analyzer (Zhejiang Li-ryder Technologies Co., Ltd., Hangzhou, China) [17]. Figure 1b shows the polarization-electric field (P-E) hysteresis loop of 8 nm AFE $Hf_{0.2}Zr_{0.8}O_2$ capacitors.

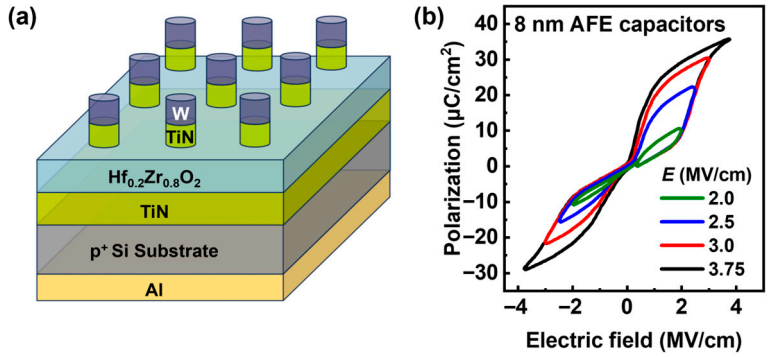



**Figure 1.** (**a**) The schematic structure of $Hf_{0.2}Zr_{0.8}O_2$ AFE devices used in this study. (**b**) *P-E* loop of 8 nm AFE $Hf_{0.2}Zr_{0.8}O_2$ capacitors under different electric fields.

### *2.2. Characterization Method*

To ensure an accurate performance evaluation and mitigate the impact of the negative voltage in the test waveform on the recovery behaviors of the device under test, a double positive-negative (PN) waveform was adopted. In this configuration, each polarization characterization cycle consists of one positive triangle pulse and one negative triangle pulse. For data analysis, as shown in Figure 2a, the extraction begins at the smooth segment of the first cycle of the transient I-V curve, and the voltage at this point is defined as the starting voltage, $V_{start}$. From here, a complete cycle with a duration of $T$ is captured, which serves as the final test waveform segment for device analysis. The measurement waveform pattern used in this study is illustrated in Figure 2b.

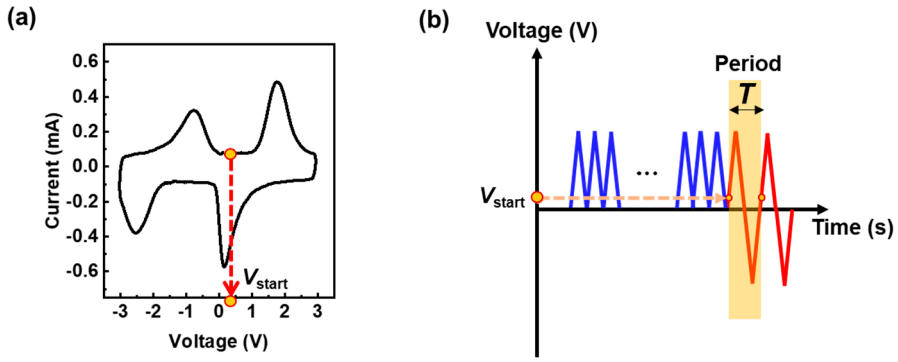



**Figure 2.** (**a**) Definition of the starting point of the smooth segment of the first transient I-V curve as $V_{start}$. (**b**) The measurement waveform pattern used in this study.

In order to systematically study the imprint evolution and recovery behavior of the device at different stages of the electrical cycling process, three consecutive endurance tests were applied to observe the imprint behavior at different stages of cycling. Subsequently, the recovery behavior of the imprint was observed under zero and negative voltage recovery conditions. Additionally, the changes in the electric domain were characterized using the FORC test. The detailed testing procedure and results will be discussed in detail in the following sections.

### *2.3. FORC Characterization*

In ferroelectric (FE) devices, the FORC test and analysis of the FORC diagram are mainly based on the Preisach model. This model conceptualizes the FE film as a collection of numerous independent, bistable "hysteresis units". Each unit represents an idealized FE domain or domain cluster with two stable polarization states ($+P_s$ and $-P_s$). The forward switching from $-P_s$ to $+P_s$ state has a switching electric field $E_s$, while the backward switching has the back-switching field $E_b$. The state of each unit is determined by the

historical electric field $E$, rather than the current field $E$. Once the state is switched to $+P_s$ with $E \geq E_s$, it will remain in the $+P_s$ state until $E < E_s$. This constitutes the microscopic physical foundation of an FE hysteresis unit. For a collection of hysteresis units, each of them has a pair of switching threshold fields ($E_s$, $E_b$), leading to a distribution function $\mu(E_s, E_b)$. From a macro perspective, when $E$ increases, the units that satisfy $E \geq E_{si}$ switch forward in batches, resulting in an increased $P$. When $E$ decreases, the units that satisfy $E \leq E_{bj}$ are switched in reverse in batches, causing $P$ to decrease. Due to the threshold separation of forward/reverse switching ($E_s \neq E_b$) and the asymmetry of the switching sequence, the FE devices exhibit a typical ferroelectric hysteresis loop when the electric field undergoes cyclic changes.

For the $Hf_{0.2}Zr_{0.8}O_2$ AFE device, as shown in Figure 3b, its typical P-E hysteresis curve is consistent with the characteristics of the hysteron in the Preisach model. This study mainly analyzes the upper loop of the AFE P-E curve (the lower loop exhibits similar characteristics). Specifically, when a forward electric field is applied starting from zero field ($E = 0$), as the applied electric field increases to $E_{\beta\alpha}$, the device undergoes a transition from the nonpolar phase to the polar phase; subsequently, when the applied electric field decreases to $E_{\alpha\beta}$, the device undergoes a transition from the polar phase to the nonpolar phase. The experimental FORC result could use (1) and (2) to convert the horizontal and vertical axes. This allows for the direct observation of the coercive field $E_c$ and the electric field bias $E_{bias}$ from the micro perspective of the AFE film [18–20].

$$E_c = \left(E_{\beta\alpha} - E_{\alpha\beta}\right) \Big/ 2 \tag{1}$$

$$E_{bias} = \left(E_{\beta\alpha} + E_{\alpha\beta}\right) \Big/ 2 \tag{2}$$

Based on the Preisach model, Figure 3c illustrates the total responses of a collection of basic hysteresis units of the $Hf_{0.2}Zr_{0.8}O_2$ AFE device under the electric field $E(t)$. In this model, the Preisach weight factor $\mu(a_i, b_i)$ reflects the interactions between domains in the AFE film. This weight factor is determined by microscopic mechanisms such as electrical coupling, mechanical stress, and defect pinning, and plays a crucial role in the overall macroscopic polarization switching behavior. The polarization response of each hysteron unit is weighted and superimposed, resulting in the P-E loop shown here [9]. The total polarization is calculated by

$$P(E) = \iint \mu(E_{\beta\alpha},\ E_{\alpha\beta}) P_{E_{\beta\alpha}, E_{\alpha\beta}}[E(t)] dE_{\beta\alpha} dE_{\alpha\beta} \tag{3}$$

Figure 3a shows an example of the applied waveform for the FORC test on the AFE device. The saturation electric field $E_{sat}$ during the FORC waveform is 3.75 MV/cm, which corresponds to a maximum voltage of 3 V for the 8 nm $Hf_{0.2}Zr_{0.8}O_2$ AFE device. To obtain a FORC diagram with enough resolution and low noise, the step of reversal field $E_r$ should be carefully chosen. In this study, the reversal voltage step size is 0.1 V and the edges of triangular waveforms are 10 μs. The detailed process of the FORC test is as follows. First, the maximum voltage of 3 V is applied. Then the voltage is reduced to the first reversal voltage of 2.9 V through a 10 μs falling edge. Subsequently, it returns to the 3 V maximum voltage with a 10 μs rising edge. This procedure continues stepwise until the reversal voltage reaches −3 V, with 60 reversal voltage steps.

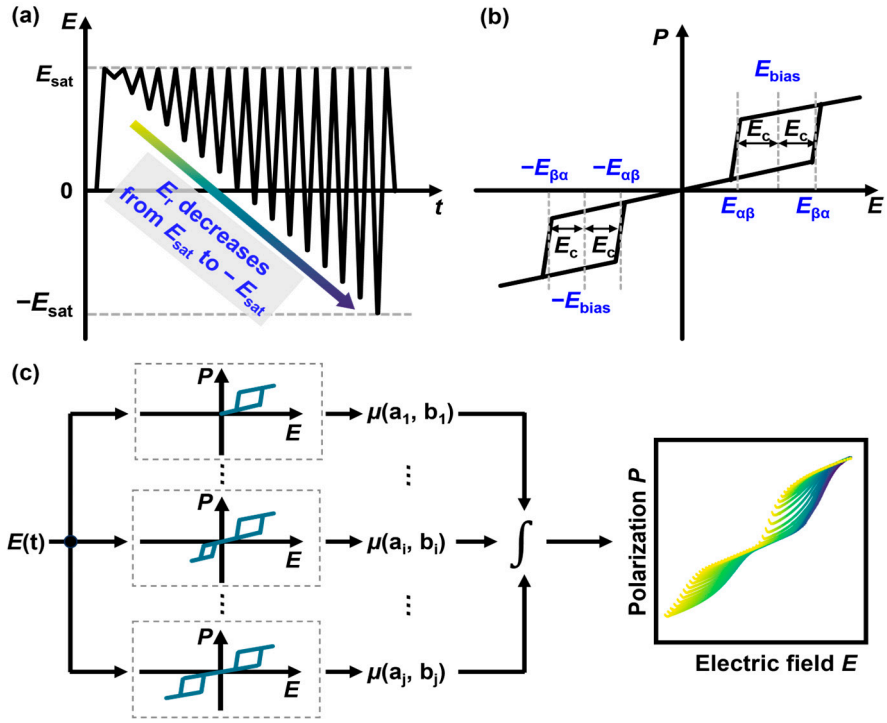



**Figure 3.** (**a**) The applied waveform for the FORC test. A reversal field $E_r$ decreases from the saturation field $E_{sat}$ to $-E_{sat}$ at equal steps. (**b**) The coercive field $E_c$ and the built-in bias electric field $E_{bias}$ in the *P*-*E* loop. The electric field $E_{\beta\alpha}$ is for the nonpolar to the polar phase transition; $E_{\alpha\beta}$ is for the polar-to-nonpolar phase transition. (**c**) The basic hysteresis unit of the $Hf_{0.2}Zr_{0.8}O_2$ AFE device and the resulting *P*-*E* hysteresis loop under the applied electric field *E*. Here, $\mu(a_i, b_i)$ and $\mu(a_j, b_j)$ are the distribution functions corresponding to the i-th and j-th hysterons in the AFE, respectively.

## 3. Results and Discussion

### *3.1. Variations in Imprint Behaviors*

During the endurance test on the $Hf_{0.2}Zr_{0.8}O_2$ AFE device with 3 V stress, different rates of imprint shifting were observed. When the pristine device undergoes endurance cycling with 10 μs and 3 V positive triangular stress, the rate of voltage shift in the transient I-V curve significantly decreases after reaching a certain level (as shown in Figure 4). Further tests indicate that the device enters the imprint slow shifting phase after approximately $10^7$ cycles of 3 V stress, which, for convenience, is referred to as the imprint weak state.

To investigate the variations in imprint behaviors in the AFE device, the pristine device was subjected to three consecutive endurance tests. Each test consisted of $10^7$ cycles at 3 V, with the test waveform shown in Figure 4a. Figure 5a presents the P-V curve of the AFE device during the first $10^7$ cycles, and the maximum polarization of the upper loop ($P_{s,max}$) is extracted at 3 V. As shown in Figure 5b, the initial $P_{s,max}$ value is slightly lower, which is attributed to the incomplete switching of domains within the AFE thin film under the ±3 V test voltage; the corresponding transient I-V characteristic curve is displayed in Figure 5c. Meanwhile, the variation in $P_{s,max}$ across the three cycling tests is less than 1.5 μC/cm$^2$ (as shown in Figure 5b), consistent with previous research [21–24]. This indicates that there has been no significant degradation in polarization performance. The observed voltage shift (in Figure 5c) is primarily attributed to the imprint behavior, rather than being dominated by the wake-up effect.

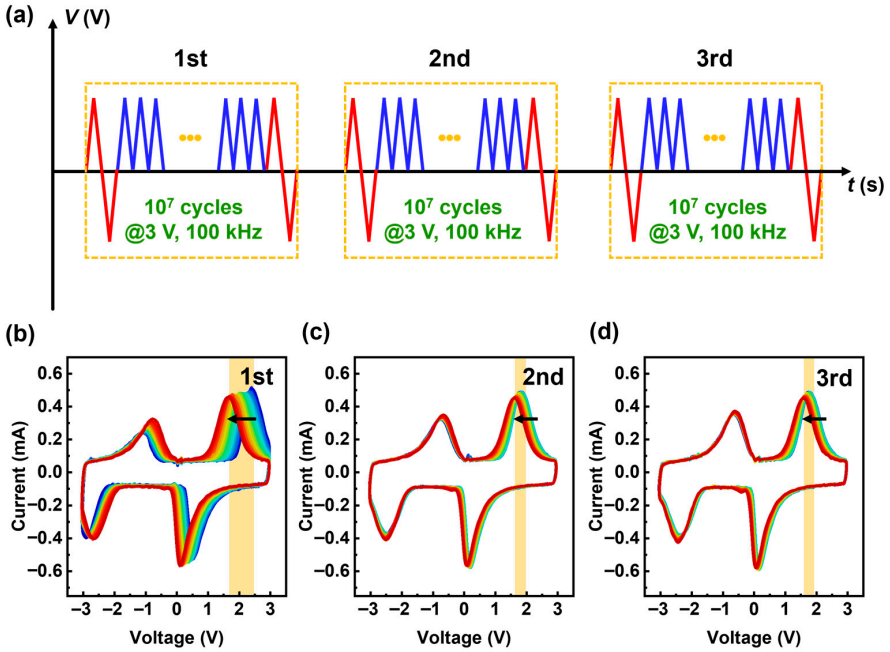



**Figure 4.** Cycling characteristics of the AFE device: (**a**) The test waveform for three consecutive cycles, each consisting of $10^7$ cycles, applied to the pristine capacitor at 3 V. The waveform is triangular with a 10 µs rise/fall time. (**b**) The transient I-V curve of the first cycle shows a significantly larger forward peak voltage shift compared to the second (**c**) and third (**d**) cycles.

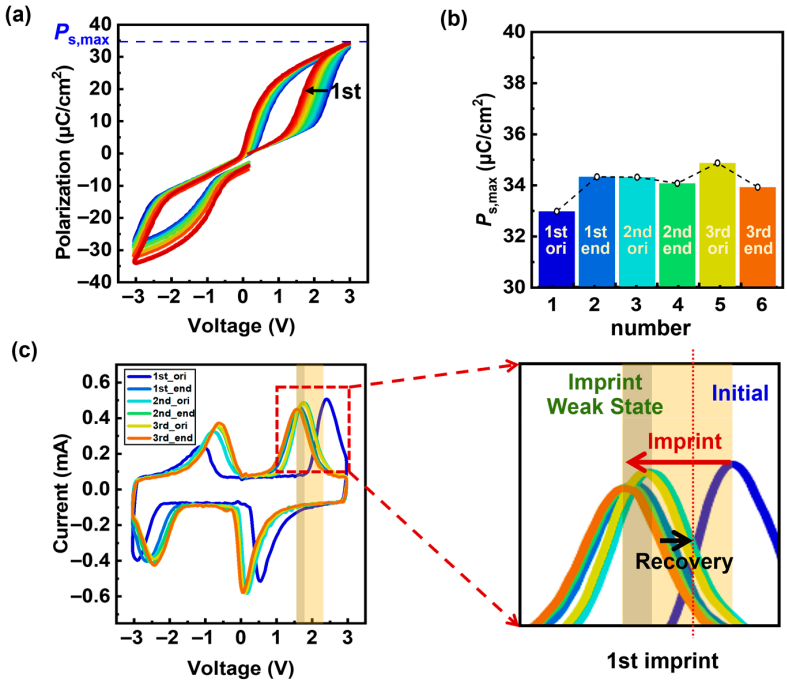



**Figure 5.** Cycling characteristics of the AFE device at room temperature: (**a**) The P-V curve of the AFE device during the first $10^7$ cycles, with the maximum polarization ($P_{s,max}$) extracted from the upper loop. (**b**) The variation in $P_{s,max}$ between the three consecutive $10^7$ cycle tests at 3 V remains below 1.5 µC/cm$^2$. (**c**) Comparison of transient I-V curves from the three $10^7$ cycle tests at 3 V, showing that the upper loop peak voltage shift in the first cycle is significantly larger than that in the second and third tests. After removing the external electric field and waiting for 500 s, a slight rightward shift in the upper loop peak voltage is observed, demonstrating the recovery behavior of the imprint.

Following the initial cycling at 3 V for $10^7$ cycles, the second and third tests, conducted under identical conditions ($10^7$ cycles of 3 V stress), showed only a minor leftward shift

in the upper loop peak voltage in the transient I-V curve (in Figure 4c,d). This indicates that the AFE device still exhibited the imprint behavior, but with significantly reduced intensity, the AFE device entered an imprint weak state (as shown in Figure 5c). Specifically, as shown in Figure 5c, the leftward shift in the upper loop peak voltage (corresponding to the position of maximum AFE domain reversal) in the first cycle was significantly larger than that in the second and third cycles. This indicates that the imprint behavior was most pronounced during the initial $10^7$ cycles under 3 V stress on the pristine device. In addition, upon removal of the external electric field, a small rightward shift is observed in the upper loop peak voltage of the transient I-V curve. This indicates imprint recovery behavior. The detailed testing of the imprint recovery will be investigated in the next section.

To explain the complex imprint behaviors of the AFE device under the 3V external electric field cycling, existing literature can be referenced. Zhou, Y.C. et al. measured the lattice spacing variation using X-ray diffraction (XRD) to calculate residual stress [23], and further discussed the impact of residual stress on the performance of the ferroelectric thin film. G. Catalan et al. reported that the flexoelectric effect influences the dielectric properties of the ferroelectric thin film under non-uniform strain [24]. They suggested that lattice mismatch induces stress at the bottom of the film, which leads to strain relaxation and creates a strain gradient within the film. Consequently, the coupling between polarization and this strain gradient results in the imprint behavior. Lee, J.K. et al. observed the dynamic domain wall motion during the polarization switching process in the ferroelectric capacitor in real-time using Transmission Electron Microscopy (TEM) [25], and proposed that the nucleation of new domains preferentially occurs at the electrode interface. E. L. Colla et al. proposed [26–28] that during low-frequency cycling, domain walls are pinned within the bulk of the film, which is in agreement with the domain wall pinning model. In contrast, during high-frequency cycling, the behavior aligns with the domain nucleation inhibition model. In this model, under the high-frequency electric field cycling, the nucleation process of some reversed domains is suppressed in the seed state, leading to the imprint effect.

Based on the existing literature and experimental observations, the possible explanations for the imprint behaviors are as follows: this phenomenon arises from non-uniform stress distribution induced by lattice mismatch, leading to elevated stress concentration at the electrode/AFE-film interface [23,24]. Furthermore, as shown in Figure 6a, after the positive electric field application, down-polarized seed domains form, which enhance the growth of down-polarized electric domains (in Figure 6b). This polarization behavior, dominated by the high-density seed domains near both electrodes, allows the AFE film to complete polarization reversal under smaller stress during subsequent positive electric field applications [25,29]. In essence, it is believed that the initial imprint behavior of the pristine AFE device under positive external electric fields is predominantly governed by the polarization dynamics facilitated by seed domains near both electrodes.

In the imprint weak state, under the influence of a positive external electric field, the piezoelectric field generated by domain walls drives the formation of oxygen vacancy defects (structural defects) within the AFE film [30]. Captured electrons accumulate near domain walls (interfaces) to lower the AFE domain wall energy [31]. The inherent electrostatic potential difference of domain walls drives electrons and oxygen vacancies to accumulate on opposite sides [32], thereby forming defect dipoles. These defect dipoles reorient along the applied electric field direction [33], ultimately leading to domain wall pinning [34]. The resulting space charge functions analogously to a local built-in electric field, thus triggering the imprint effect [35]. In essence, it is believed that the imprint behavior of the AFE device under positive electric fields, after reaching the imprint weak state, is primarily governed by domain wall pinning caused by structural defects (as shown in Figure 6b).

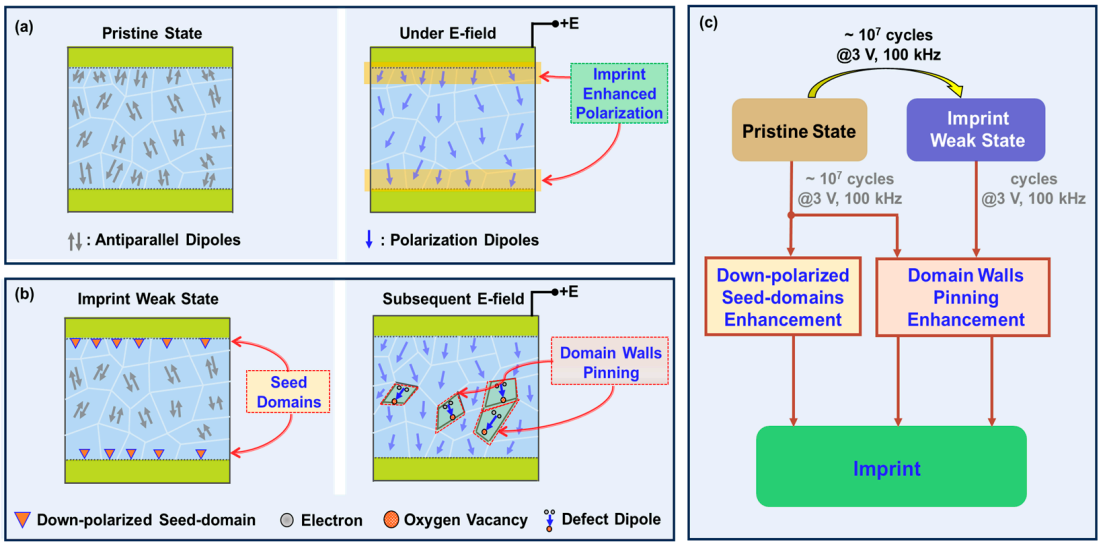



**Figure 6.** Mechanisms of the evolution of imprint behaviors in the AFE device. (**a**) Imprint behavior in the initial state: After approximately $10^7$ cycles of the positive electric field at 3 V, the device enters a weak imprint state. During this process, down-polarized seed domains are retained at both electrodes, and partial domain pinning is induced by a small number of defect dipoles within the film. (**b**) Imprint behavior in the imprint weak state: Continued application of the positive electric field cycles in the imprint weak state increases the number of defect dipoles in the film, enhancing the domain pinning effect. (**c**) Summary of the mechanisms of the imprint effect.

### *3.2. Imprint Behavior and Recovery Mechanisms*

The sub-cycling behavior refers to the phenomenon where the applied cycling voltage falls within the reversible switching region of AFE domains. This causes local charge rearrangement and defect migration within the AFE film. As a result, a local internal bias field is formed [36]. This local internal bias field causes phenomena such as P-V curve distortion and splitting up of the switching current peak in the transient I-V curve [37,38]. The mechanism of this local internal bias field is highly similar to the local imprint effect [20,39,40]. Given this similarity, the study further combines sub-cycling and FORC testing, with the applied waveform shown in Figure 7, to systematically investigate the local imprint effect and recovery behavior in AFE devices.

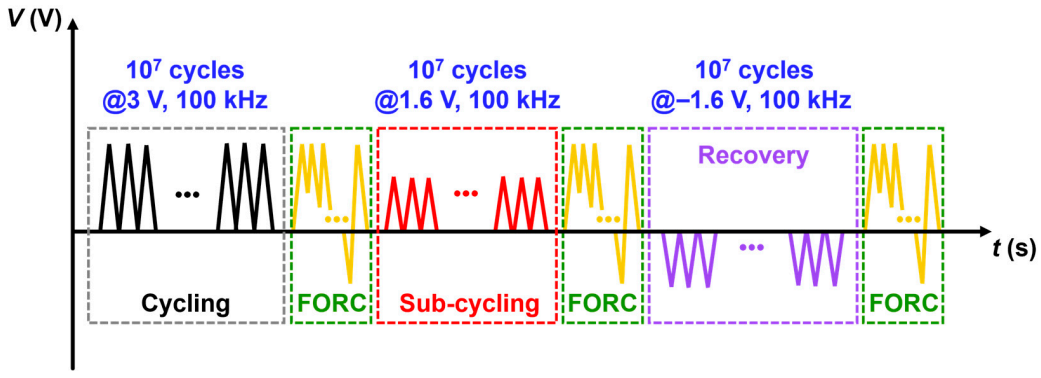



**Figure 7.** Test waveform for the local imprint behavior and recovery characteristics of the AFE device at room temperature.

At room temperature, three AFE devices in the imprint weak state were subjected to sub-cycling at 1.6 V for $10^7$ cycles, resulting in a split-up state. Their transient I-V characteristics were then measured and compared under different recovery conditions. As shown in Figure 8a, a device exhibited slight self-recovery behavior under 0 V for 500 s.

As shown in Figure 8b,c, after applying negative cyclic electric fields at −1.6 V and −2.4 V for $10^7$ cycles, the imprint recovery of each device exceeded that observed in the imprint weak state.

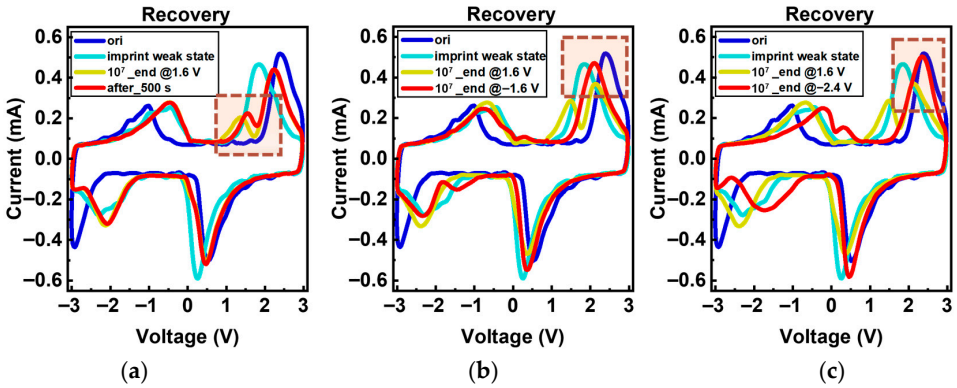



**Figure 8.** Comparison of transient I-V characteristics of AFE devices at room temperature following splitting up induced by $10^7$ sub-cycles at 1.6 V stress, under different recovery voltage treatments: (**a**) waiting 500s at 0 V. (**b**) $10^7$ cycles of −1.6 V stress. (**c**) $10^7$ cycles of −2.4 V stress.

The FORC test results of the AFE device at room temperature are shown in Figure 9. Figure 9e–h correspond to Figure 9a–d and display the evolution of the coercive voltage $V_c$ and the internal bias voltage $V_{bias}$ distributions under different states of the device. In the pristine state (as shown in Figure 9e), $V_c$ is dispersed around 1.25 V, 0.8 V, and 0.75 V, while $V_{bias}$ is distributed around 1.6 V, 1.45 V, and 1.1 V, consistent with Figure 9a. This indicates a dispersed distribution of domains within the film. After the external electric field cycling, the AFE reaches an imprint weak state, and the FORC diagram transitions to a concentrated distribution (in Figure 9b). Corresponding to Figure 9f, the distribution of $V_c$ and $V_{bias}$ concentrates around 0.8 V and 1.1 V, suggesting that the imprint behavior drives domain rearrangement, leading to a transition of the domains to a more concentrated distribution [41].

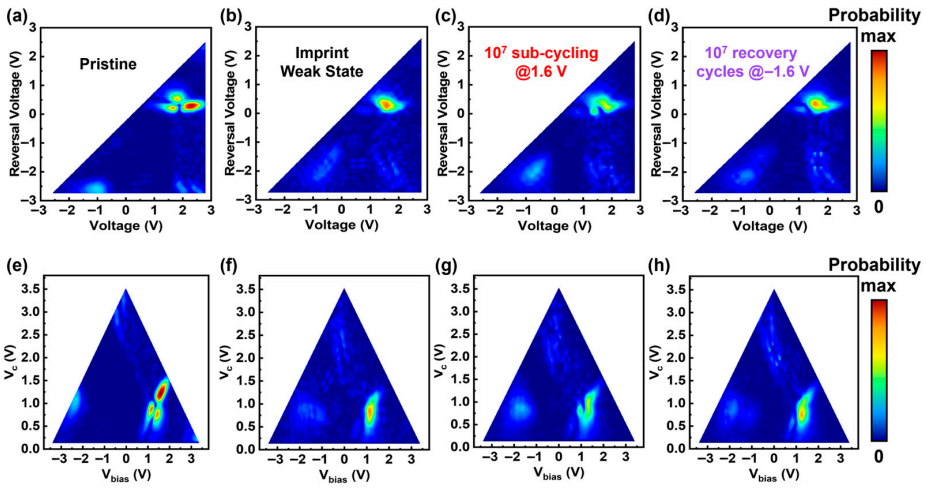



**Figure 9.** (**a**) The pristine state. (**b**) After applying $10^7$ cycles of 3 V stress to the AFE devices at room temperature, the device enters the imprint weak state. (**c**) Subsequent application of 1.6 V stress for $10^7$ sub-cycles induces the split-up phenomenon. (**d**) After applying recovery sub-cycles of $10^7$ at –1.6 V stress, the FORC diagram indicates that structural defects are largely recovered, while movable defects remain and have not returned to their pristine state. (**e**–**h**) corresponding to the coercive voltage $V_c$ and internal bias voltage $V_{bias}$ distribution maps for (**a**–**d**).

Under sub-cycling at 1.6 V for $10^7$ cycles, the voltage distribution splits up again. As shown in Figure 9g, two peaks appear in the $V_c$ at 0.8 V and 0.9 V, while the $V_{bias}$ splits up into two peaks at 1.4 V and 1.0 V. This is consistent with the temporary dispersion of the domain distribution shown in the FORC diagram in Figure 9c. At this point, the AFE domains cannot fully switch. The domains activated at this sub-cycling voltage form locally switchable regions [19], generating localized high electric fields at the interfaces with unswitched domains. These high electric fields distort and weaken the polar molecular bonds, promoting bond breakage and thereby accelerating the generation of oxygen vacancies [42], which further enhances the pinning effect of defect dipoles at domain walls. The expansion of these local regions strengthens the local imprint effect, which is reflected in the FORC diagram as a temporary dispersion of the AFE domain distribution.

After applying the recovery cycling at $-1.6$ V for $10^7$ cycles, the $V_c$ and $V_{bias}$ again concentrate around 0.75 V and 1.25 V, respectively, as shown in Figure 9h. The AFE thin film system returns to a more uniform state, and this trend is consistent with the recovery results in the FORC diagram (in Figure 9d). Due to the altered distribution of movable defects in the AFE film compared to the original state, the FORC diagram in Figure 9d cannot fully revert to the original dispersed distribution of the device.

When the AFE film undergoes polarization, the centers of positive and negative charges within the unit cells shift along the electric field direction, forming electric dipole moments. The polarization direction points from the negative charge center to the positive charge center. Under the forward electric field, bound charges at domain interfaces are primarily compensated by the applied field, balancing defect dipoles pinned at domain walls. Simultaneously, the external electric field drives the rupture of Hf-O/Zr-O bonds, generating $O^{2-}$ ions [43]. These ions drift toward the electrodes, leaving oxygen vacancies at their original sites. Raghavan, N et al. [44] proposed that materials such as TiN electrodes can act as "oxygen reservoirs", absorbing and storing migrating $O^{2-}$ ions during breakdown, while themselves being resistant to oxidation. According to secondary ion mass spectrometry (SIMS) analysis by Migita, S. et al. [45], the oxygen content at the electrode interface of the $HfO_2$ ferroelectric thin film is higher than that within the bulk of the film.

It is hypothesized that the TiN electrode, owing to its high oxygen solubility, stores $O^{2-}$ ions without reacting with them. Upon removal of the external electric field (zero-voltage state), the stored $O^{2-}$ ions migrate back to balance the defect dipoles, triggering a spontaneous de-trapping process. This process transforms defect dipoles into polarized dipoles, reorienting them from ordered to random configurations. Consequently, the local built-in electric field strength at domain boundaries diminishes, weakening the domain pinning effect and ultimately achieving self-recovery of the imprint effect (as shown in Figures 8a and 10a).

Under the influence of negative cyclic electric fields, the recombination of $O^{2-}$ ions released from both metal electrodes with oxygen vacancy defects is accelerated. This facilitates the passivation of oxygen vacancy traps and the formation of lattice oxygen atoms [46]. Concurrently, the number of imprint seed domains with downward polarization near the electrodes decreases. This phenomenon is speculated to originate from the imprint recovery mechanism dominated by the negative electric field, which enables imprint recovery by reducing the number of downward-polarized imprint seed domains near both electrodes (as shown in Figure 10b).

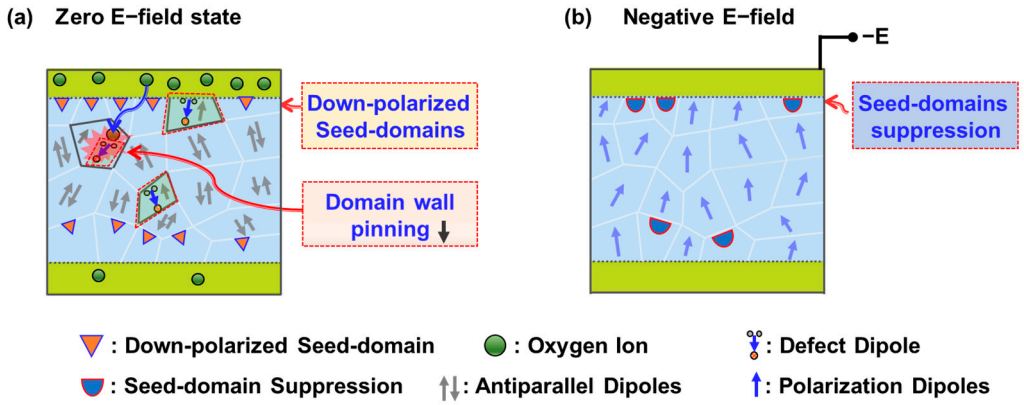



**Figure 10.** Mechanisms of the evolution of imprint recovery behaviors in the AFE device. (**a**) The self-recovery of imprint effect under zero electric field: Oxygen ions stored at the TiN electrode migrate back, transforming defect dipoles into polarization dipoles. (**b**) Imprint recovery behavior under the reverse cycling electric field: Downward-polarized seed domains near the electrodes decrease and are suppressed; concurrently, the number of defect dipoles in the AFE film reduces, weakening the domain pinning effect. These changes collectively result in significant attenuation of the imprint effect.

## 4. Conclusions

This study investigated the dynamic imprint and recovery effects in the $Hf_{0.2}Zr_{0.8}O_2$ AFE thin film. For the pristine device, imprint is governed by seed domains near both electrodes. However, at a reduced voltage shift speed, the imprint is dominated by domain pinning induced by defect dipoles. By integrating FORC analysis with sub-cycling characterization, this study has quantified the coercive field, internal bias field, and domain distribution within the AFE thin film. Based on these findings, possible physics-based mechanisms have been discussed to explicate the imprint and recovery behaviors, providing new insights for optimizing performance and enhancing the reliability of AFE memories.

**Author Contributions:** Conceptualization, Y.H. and Y.Q.; methodology, Y.H. and Z.W.; software, Y.H. and J.L.; validation, Y.H., J.L. and L.C.; formal analysis, Y.H. and Y.Q.; investigation, Y.H.; resources, Y.D.; data curation, Y.H.; writing—original draft preparation, Y.H.; writing—review and editing, Y.H. and Y.Q.; visualization, Y.Q. and Y.H.; supervision, Y.Q.; project administration, Y.Q. and Y.Z.; funding acquisition, Y.Z., Y.Q. and J.Q. All authors have read and agreed to the published version of the manuscript.

**Funding:** This research was funded by the National Natural Science Foundation of China under Grant 62204086, and by the ZJU-HDSC Joint Research Center.

**Data Availability Statement:** The original contributions presented in this study are included in the article. Further inquiries can be directed to the corresponding author.

**Conflicts of Interest:** Authors Jianguo Li, Lijian Chen, Jiabin Qi, Yiming Qu and Yi Zhao were employed by the company Huada Semiconductor Co., Ltd. The remaining authors declare that the research was conducted in the absence of any commercial or financial relationships that could be construed as a potential conflict of interest.

## References

1. Vishnumurthy, P.; Alcala, R.; Mikolajick, T.; Schroeder, U.; Antunes, L.A.; Kersch, A. ferroelectric $HfO_2$-based capacitors for FeRAM: Reliability from field cycling endurance to retention (invited). In Proceedings of the 2024 IEEE International Reliability Physics Symposium (IRPS), Dallas, TX, USA, 14 April 2024; IEEE: Grapevine, TX, USA, 2024; pp. 1–10.
2. Bouaziz, J.; Rojo Romeo, P.; Baboux, N.; Vilquin, B. Imprint issue during retention tests for $HfO_2$-based FRAM: An industrial challenge? *Appl. Phys. Lett.* **2021**, *118*, 082901. [CrossRef]

3. Sünbül, A.; Lehninger, D.; Lederer, M.; Mähne, H.; Hoffmann, R.; Bernert, K.; Thiem, S.; Schöne, F.; Döllgast, M.; Haufe, N.; et al. A study on imprint behavior of ferroelectric hafnium oxide caused by high-temperature annealing. *Phys. Status Solidi A* **2023**, *220*, 2300067. [CrossRef]
4. Mulaosmanovic, H.; Lomenzo, P.D.; Schroeder, U.; Slesazeck, S.; Mikolajick, T.; Max, B. Reliability aspects of ferroelectric hafnium oxide for application in non-volatile memories. In Proceedings of the 2021 IEEE International Reliability Physics Symposium (IRPS), Monterey, CA, USA, 21–24 March 2021; IEEE: Monterey, CA, USA, 2021; pp. 1–6.
5. Warren, W.L.; Tuttle, B.A.; Dimos, D.; Pike, G.E.; Al-Shareef, H.N.; Ramesh, R.; Evans, J.T.; Jr, J. Imprint in ferroelectric capacitors. *JPN. J. Appl. Phys.* **1996**, *35*, 1521. [CrossRef]
6. Takada, K.; Takarae, S.; Shimamoto, K.; Fujimura, N.; Yoshimura, T. Time-dependent imprint in $Hf_{0.5}Zr_{0.5}O_2$ ferroelectric thin films. *Adv. Electron. Mater.* **2021**, *7*, 2100151. [CrossRef]
7. Chojecki, P.; Walters, G.; Forrester, Z.; Nishida, T. Preisach modeling of imprint on hafnium zirconium oxide ferroelectric capacitors. *J. Appl. Phys.* **2021**, *130*, 094102. [CrossRef]
8. Alhada-Lahbabi, K.; Manchon, B.; Magagnin, G.; Lepri, C.; Gonzalez, S.; Infante, I.C.; Le Berre, M.; Vilquin, B.; Bouaziz, J.; Gautier, B.; et al. Investigating experimental short term imprint dynamics in ferroelectric hafnium oxide through phase-field modeling. *Adv. Funct. Mater.* **2025**, e14094. [CrossRef]
9. Buragohain, P.; Erickson, A.; Kariuki, P.; Mittmann, T.; Richter, C.; Lomenzo, P.D.; Lu, H.; Schenk, T.; Mikolajick, T.; Schroeder, U.; et al. Fluid imprint and inertial switching in ferroelectric La:$HfO_2$ capacitors. *ACS Appl. Mater. Interfaces* **2019**, *11*, 35115–35121. [CrossRef]
10. Pesic, M.; Schroeder, U.; Slesazeck, S.; Mikolajick, T. Comparative study of Reliability of ferroelectric and anti-ferroelectric memories. *IEEE Trans. Device Mater. Reliab.* **2018**, *18*, 154–162. [CrossRef]
11. Hsiang, K.-Y.; Liao, C.-Y.; Lin, Y.-Y.; Lou, Z.-F.; Lin, C.-Y.; Lee, J.-Y.; Chang, F.-S.; Li, Z.-X.; Tseng, H.-C.; Wang, C.-C.; et al. Correlation between access polarization and high endurance (~$10^{12}$ cycling) of ferroelectric and anti-ferroelectric $HfZrO_2$. In Proceedings of the 2022 IEEE International Reliability Physics Symposium (IRPS), Dallas, TX, USA, 27–31 March 2022; IEEE: Dallas, TX, USA, 2022; pp. P9-1–P9-4.
12. Yuan, P.; Mao, G.-Q.; Cheng, Y.; Xue, K.-H.; Zheng, Y.; Yang, Y.; Jiang, P.; Xu, Y.; Wang, Y.; Wang, Y.; et al. Microscopic mechanism of imprint in hafnium oxide-based ferroelectrics. *Nano Res.* **2022**, *15*, 3667–3674. [CrossRef]
13. Pešić, M.; Fengler, F.P.G.; Larcher, L.; Padovani, A.; Schenk, T.; Grimley, E.D.; Sang, X.; LeBeau, J.M.; Slesazeck, S.; Schroeder, U.; et al. Physical mechanisms behind the field-cycling behavior of $HfO_2$-based ferroelectric capacitors. *Adv. Funct. Mater.* **2016**, *26*, 4601–4612. [CrossRef]
14. Peng, H.-K.; Chiu, C.-Y.; Kao, Y.-C.; Wu, P.-J.; Wu, Y.-H. Enhanced reliability, switching speed and uniformity for ferroelectric $HfZrO_x$ on epitaxial Ge film by post deposition annealing for oxygen vacancy control. *IEEE Trans. Electron Devices* **2022**, *69*, 4002–4009. [CrossRef]
15. Kang, M.; Peng, Y.; Xiao, W.; Zhang, Y.; Wang, Z.; Du, P.; Jiang, H.; Liu, F.; Liu, Y.; Hao, Y.; et al. $HfO_2$–$ZrO_2$ ferroelectric capacitors with superlattice structure: Improving fatigue stability, fatigue recovery, and switching speed. *ACS Appl. Mater. Interfaces* **2024**, *16*, 2954–2963. [CrossRef]
16. Weng, Z.; Zhao, L.; Lee, C.; Zhao, Y. Phase transitions and anti-ferroelectric behaviors in $Hf_{1-x}Zr_xO_2$ films. *IEEE Electron Device Lett.* **2023**, *44*, 1780–1783. [CrossRef]
17. Zhejiang Liryder Technologies Co., Ltd. Available online: https://www.liryder.com/en/ (accessed on 4 September 2025).
18. Shi, Z.; Zhou, D.; Li, S.; Xu, J.; Schroeder, U. First-order reversal curve diagram and its application in investigation of polarization switching behavior of $HfO_2$-based ferroelectric thin films. *Acta Phys. Sin.* **2021**, *70*, 127702. [CrossRef]
19. Li, S.; Zhou, D.; Shi, Z.; Hoffmann, M.; Mikolajick, T.; Schroeder, U. Involvement of unsaturated switching in the endurance cycling of Si-doped $HfO_2$ ferroelectric thin films. *Adv. Electron. Mater.* **2020**, *6*, 2000264. [CrossRef]
20. Schenk, T.; Hoffmann, M.; Ocker, J.; Pešić, M.; Mikolajick, T.; Schroeder, U. Complex internal bias fields in ferroelectric hafnium oxide. *ACS Appl. Mater. Interfaces* **2015**, *7*, 20224–20233. [CrossRef]
21. Ding, Y.; Huo, Y.; Yan, C.; Weng, Z.; Li, J.; Lan, Z.; Qu, Y.; Zhao, Y. Modeling of endurance degradation of anti-ferroelectric $Hf_{1-x}Zr_xO_2$ capacitors. In Proceedings of the 2024 Conference of Science and Technology for Integrated Circuits (CSTIC), Shanghai, China, 17–18 March 2024; IEEE: Shanghai, China, 2024; pp. 1–3.
22. Chen, L.; Ding, Y.; Weng, Z.; Li, J.; Cai, D.; Zhao, Y. A compact model for degradation behaviors in $Hf_{0.2}Zr_{0.8}O_2$ anti-ferroelectric devices. *IEEE Trans. Electron Devices* **2025**, *72*, 2936–2942. [CrossRef]
23. Zhou, Y.C.; Yang, Z.Y.; Zheng, X.J. Residual stress in PZT thin films prepared by pulsed laser deposition. *Surf. Coat. Technol.* **2003**, *162*, 202–211. [CrossRef]
24. Catalan, G.; Sinnamon, L.J.; Gregg, J.M. The effect of flexoelectricity on the dielectric properties of inhomogeneously strained ferroelectric thin films. *J. Phys. Condens. Matter* **2004**, *16*, 2253–2264. [CrossRef]
25. Lee, J.K.; Shin, G.Y.; Song, K.; Choi, W.S.; Shin, Y.A.; Park, S.Y.; Britson, J.; Cao, Y.; Chen, L.-Q.; Lee, H.N.; et al. Direct observation of asymmetric domain wall motion in a ferroelectric capacitor. *Acta Mater.* **2013**, *61*, 6765–6777. [CrossRef]

26. Colla, E.L.; Tagantsev, A.K.; Taylor, D.V.; Kholkin, A.L. Fatigued state of the Pt-PZT-Pt system. *Integr. Ferroelectr.* **1997**, *18*, 19–28. [CrossRef]
27. Colla, E.L.; Taylor, D.V.; Tagantsev, A.K.; Setter, N. Discrimination between bulk and interface scenarios for the suppression of the switchable polarization (fatigue) in Pb(Zr,Ti)$O_3$ thin films capacitors with Pt electrodes. *Appl. Phys. Lett.* **1998**, *72*, 2478–2480. [CrossRef]
28. Taylor, D.V.; Damjanovic, D.; Colla, E.; Setter, N. Fatigue and nonlinear dielectric response in sol-gel derived lead zirconate titanate thin films. *Ferroelectrics* **1999**, *225*, 91–97. [CrossRef]
29. Tagantsev, A.K.; Stolichnov, I.; Colla, E.L.; Setter, N. Polarization fatigue in ferroelectric films: Basic experimental findings, phenomenological scenarios, and microscopic features. *J. Appl. Phys.* **2001**, *90*, 1387–1402. [CrossRef]
30. Wen, X.-Y.; Yu, J.; Ren, T.-L.; Xue, K.-H.; Zhou, W.-L.; Wang, Y.-B. Studies on the fatigue behavior of ferroelectric film using preisach approach. *Integr. Ferroelectr.* **2008**, *99*, 3–12. [CrossRef]
31. Postnikov, V.S.; Pavlov, V.S.; Turkov, S.K. Internal friction in ferroelectrics due to interaction of domain boundaries and point defects. *J. Phys. Chem. Solids* **1970**, *31*, 1785–1791. [CrossRef]
32. Hong, L.; Soh, A.K.; Du, Q.G.; Li, J.Y. Interaction of O vacancies and domain structures in single crystal $BaTiO_3$: Two-dimensional ferroelectric model. *Phys. Rev. B* **2008**, *77*, 094104. [CrossRef]
33. Chen, K.; Yuan, X.; Tian, Z.; Zou, M.; Yuan, Y.; Chen, Z.; Zhang, Q.; Zhang, Y.; Jin, X.; Wu, T.; et al. A facile approach for generating ordered oxygen vacancies in metal oxides. *Nat. Mater.* **2025**, *24*, 835–842. [CrossRef]
34. Fengler, F.P.G.; Pešić, M.; Starschich, S.; Schneller, T.; Künneth, C.; Böttger, U.; Mulaosmanovic, H.; Schenk, T.; Park, M.H.; Nigon, R.; et al. Domain Pinning: Comparison of Hafnia and PZT Based Ferroelectrics. *Adv. Electron. Mater.* **2017**, *3*, 1600505. [CrossRef]
35. Warren, W.L.; Pike, G.E.; Dimos, D.; Vanheusden, K.; Al-Shareef, H.N.; Tuttle, B.A.; Ramesh, R.; Evans, J.T. Voltage shifts and defect-dipoles in ferroelectric capacitors. *MRS Proc.* **1996**, *433*, 257. [CrossRef]
36. Morozov, M.I.; Damjanovic, D. Hardening-softening transition in Fe-doped Pb(Zr,Ti)$O_3$ ceramics and evolution of the third harmonic of the polarization response. *J. Appl. Phys.* **2008**, *104*, 034107. [CrossRef]
37. Schenk, T.; Schroeder, U.; Pešić, M.; Popovici, M.; Pershin, Y.V.; Mikolajick, T. Electric field cycling behavior of ferroelectric hafnium oxide. *ACS Appl. Mater. Interfaces* **2014**, *6*, 19744–19751. [CrossRef] [PubMed]
38. Li, S.; Zhou, D.; Shi, Z.; Hoffmann, M.; Mikolajick, T.; Schroeder, U. Temperature-dependent subcycling behavior of Si-doped $HfO_2$ ferroelectric thin films. *ACS Appl. Electron. Mater.* **2021**, *3*, 2415–2422. [CrossRef]
39. Stancu, A.; Ricinschi, D.; Mitoseriu, L.; Postolache, P.; Okuyama, M. First-order reversal curves diagrams for the characterization of ferroelectric switching. *Appl. Phys. Lett.* **2003**, *83*, 3767–3769. [CrossRef]
40. Pešić, M.; Slesazeck, S.; Schenk, T.; Schroeder, U.; Mikolajick, T. Impact of charge trapping on the ferroelectric switching behavior of doped $HfO_2$. *Phys. Status Solidi A* **2016**, *213*, 270–273. [CrossRef]
41. Grimley, E.D.; Schenk, T.; Mikolajick, T.; Schroeder, U.; LeBeau, J.M. Atomic structure of domain and interphase boundaries in ferroelectric $HfO_2$. *Adv. Mater. Interfaces* **2018**, *5*, 1701258. [CrossRef]
42. McPherson, J.W.; Kim, J.; Shanware, A.; Mogul, H.; Rodriguez, J. Trends in the ultimate breakdown strength of high dielectric-constant materials. *IEEE Trans. Electron Devices* **2003**, *50*, 1771–1778. [CrossRef]
43. Kumari, N.; Krupanidhi, S.B.; Varma, K.B.R. Dielectric, impedance and ferroelectric characteristics of c-oriented bismuth vanadate films grown by pulsed laser deposition. *Mater. Sci. Eng. B* **2007**, *138*, 22–30. [CrossRef]
44. Raghavan, N.; Pey, K.L.; Wu, X.; Liu, W.; Li, X.; Bosman, M.; Kauerauf, T. Oxygen-soluble gate electrodes for prolonged high-k gate-stack reliability. *IEEE Electron Device Lett.* **2011**, *32*, 252–254. [CrossRef]
45. Migita, S.; Ota, H.; Yamada, H.; Shibuya, K.; Sawa, A.; Matsukawa, T.; Toriumi, A. Ion implantation synthesis of Si-doped $HfO_2$ ferroelectric thin films. In Proceedings of the 2018 IEEE 2nd Electron Devices Technology and Manufacturing Conference (EDTM), Kobe, Japan, 13–16 March 2018; IEEE: Kobe, Japan, 2018; pp. 44–46.
46. Böscke, T.S.; Müller, J.; Bräuhaus, D.; Schröder, U.; Böttger, U. Ferroelectricity in hafnium oxide thin films. *Appl. Phys. Lett.* **2011**, *99*, 102903. [CrossRef]


**Disclaimer/Publisher's Note:** The statements, opinions and data contained in all publications are solely those of the individual author(s) and contributor(s) and not of MDPI and/or the editor(s). MDPI and/or the editor(s) disclaim responsibility for any injury to people or property resulting from any ideas, methods, instructions or products referred to in the content.